# Early Formation of a Water Ocean as a Function of Initial CO 2 and H 2 O Contents in a Solidifying Rocky Planet

H. Massol, A. Davaille, P. Sarda

JGR Planets

RESEARCH ARTICLE
10.1029/2023JE007848

**Key Points:**

- An initial $CO_2$ content up to 1,000 bars would not prevent condensation of a water ocean on the early Earth
- 0.13 Earth's ocean mass would be sufficient to form a water ocean on early Venus
- Liquid water may be present on the surface of Trappist-1e and 1f

**Correspondence to:**

H. Massol,
helene.massol@universite-paris-saclay.fr

**Citation:**

Massol, H., Davaille, A., & Sarda, P. (2023). Early formation of a water ocean as a function of initial $CO_2$ and $H_2O$ contents in a solidifying rocky planet. *Journal of Geophysical Research: Planets*, *128*, e2023JE007848. https://doi.org/10.1029/2023JE007848

Received 11 APR 2023
Accepted 19 JUL 2023

**Author Contributions:**

**Conceptualization:** H. Massol, A. Davaille
**Investigation:** P. Sarda
**Methodology:** H. Massol, A. Davaille, P. Sarda
**Project Administration:** H. Massol
**Software:** H. Massol
**Visualization:** A. Davaille
**Writing – original draft:** H. Massol, P. Sarda
**Writing – review & editing:** H. Massol, A. Davaille, P. Sarda



# Early Formation of a Water Ocean as a Function of Initial $CO_2$ and $H_2O$ Contents in a Solidifying Rocky Planet

**H. Massol[1], A. Davaille[2], and P. Sarda[1]**

[1]Université Paris-Saclay, CNRS, GEOPS, Orsay, France, [2]Université Paris-Saclay, CNRS, FAST, Orsay, France

**Abstract** We present a model for the thermal evolution of Magma Ocean (MO) in interaction with a degassing atmosphere of $H_2O$ and $CO_2$. The interior model is based on parameterized convection and is coupled to the atmospheric Model of Marcq et al. (2017, https://doi.org/10.1002/2016JE005224) through heat and volatiles. A new equation for the mass balance of volatiles is implemented, correcting Salvador et al. (2017, https://doi.org/10.1002/2017je005286). We found that the domain for water condensation is extended: for instance, depending on the cloud cover and resulting albedo, 0.13 Earth's ocean mass might be sufficient to form a water ocean on early Venus (instead of 0.3 MEO in Salvador et al. (2017, https://doi.org/10.1002/2017je005286)). Comparing our results with other recent models, we discuss the relative influence of the model hypotheses, such as mantle melting curves (which depend on mantle composition), the treatment of the atmosphere (e.g., gray or convective-radiative) and the treatment of the last stages of the MO solidification (e.g., episodic resurfacing, stagnant lid…). We also apply our results to exoplanets. They suggest that liquid water might be present at the surface of Trappist-1e and 1f, provided that those planets' volatile primitive contents were dominated by $H_2O$ and $CO_2$.

**Plain Language Summary** We present a numerical model of a cooling magma ocean (MO) and the atmosphere degassing from it. The solidification of the MO leads to the enrichment of the silicate melt in volatiles, thus favoring degassing. Both reservoirs interact via heat and volatile exchange, where the volatiles are $H_2O$ and $CO_2$. The aim of this model is to explore the influence of the atmosphere on the surface conditions after the MO stage, and especially the conditions required for the condensation of a water ocean to occur. For example, for an early Earth at 1 AU initially containing 1 Earth's water ocean mass, a water ocean could form for initial $CO_2$ content as large as 1,000 bars. Moreover, a tenth of the actual Earth's water ocean mass would be sufficient to generate a water ocean on early Venus. Liquid water could also be present on the surface of the two exoplanets Trappist-1e and 1f. Comparing our results with other recent models, we discuss the relative influence of the model hypotheses, such as mantle composition, the treatment of the heat transfer in the atmosphere, and the treatment of the last stages of the MO solidification.

## 1. Introduction

Planetary habitability depends on the presence of liquid water on the planetary surface. To predict under which conditions water oceans can form, and to detect liquid water in planetary systems, are two of the key questions of planetary and exo-planetary sciences. On the observational side, our times are very exciting, with the development of new spectral techniques and analyses (e.g., Ryan & Robinson, 2022), using telescopes such as Kepler launched in 2009, CHEOPS (CHaracterising ExOPlanet Satellite) in 2019, or the more recent JWST (James Webb Space Telescope) in 2022. They made possible the recent discovery of thousands of exoplanets and pave the way to the characterization of their atmospheres and surfaces. However, we cannot study in detail all discovered exoplanets. So looking for habitability requires narrowing down the exoplanets to investigate, and therefore to understand the conditions permitting water ocean formation and sustainability. To this end, two types of models have been developed.

1D models coupling the evolution of the silicate planet to its atmosphere have investigated the early stages of planetary cooling with the solidification of the initial magma ocean (hereafter MO) triggering atmosphere formation and possibly water ocean formation (Abe, 1997; Bower et al., 2019; Elkins-Tanton, 2008; Hamano et al., 2013; Lebrun et al., 2013; Lichtenberg et al., 2021; Nikolaou et al., 2019; Salvador et al., 2017). The latter depends on the incoming solar flux (therefore on the type of star and the distance star-planet), the heat flux out of the convective planetary mantle, the oxydation of the MO (Gaillard et al., 2021, 2022), the type and quantity of

volatiles initially dissolved in the MO and exsolved to the atmosphere (Gaillard et al., 2022; Lichtenberg, 2021), the atmospheric escape (Hamano et al., 2013), the albedo, the presence of clouds, and the way atmosphere dynamics are modeled (gray or *k*-correlated radiation, radiative or radiative-convective,…).

More recently, 3D Global Circulations Models (GCM) focused on the sustainability of an existing water ocean ("aqua" planet) or at least pockets of liquid water ("land" or "dry" planet) on the planetary surface (Abe et al., 2011; Leconte et al., 2013; Turbet et al., 2021; Way & Del Genio, 2020; Way et al., 2016; Yang et al., 2014, 2019). These models are not coupled with interior dynamics, but they make it possible to investigate the influence of the planet's rotation, the planet topography, and the 3D distribution of clouds, on liquid water existence and survival as the incoming stellar flux increases through time.

In a series of papers (Lebrun et al., 2013; Salvador et al., 2017, hereafter "S2017"), we developed a parameterized 1D thermal evolution model coupling planetary mantle and atmosphere dynamics, aiming at investigating the influence of $H_2O/CO_2$ atmospheres on surface conditions at the end of the initial MO phase. Unfortunately, we made a mistake in the volatile mass balance which necessitates a correction of our previous model to see the implications (a) on the state of the surface after the MO stage and (b) on the duration of the MO Stage. This mistake pointed out in Bower et al. (2019) (hereafter B2019), also appears in other coupled MO-atmosphere studies (e.g., Elkins-Tanton, 2008; Nikolaou et al., 2019).

So, in this paper, we first correct the volatile mass balance of S2017 and show how it affects the S2017 results. We then compare our new results to other 1D and 3D recent models. Last, we use our results to discuss the early evolution of Venus as well as the state of the surface of different exoplanets.

## 2. Coupled Atmosphere-MO Model

### 2.1. Correction of the Volatiles Mass Balance

We consider that $k$ volatile species are initially dissolved in the MO. The mass balance for each volatile species $i$ ($i = 1{:}\ k$) within the whole MO—atmosphere system is ensured by mass conservation, which writes (Appendix C from S2017):

$$M_i^{\text{solid}} + M_i^{\text{liquid}} + M_i^{\text{atm}} = X_{i,t=0} M_{t=0}^{\text{MO}}, \tag{1}$$

where $M_i^{\text{solid}}$, $M_i^{\text{liquid}}$, and $M_i^{\text{atm}}$ are the masses of each volatile species (subscript $i$) in the solidified mantle, in the molten part, and the atmosphere respectively. $X_{i,t=0}$ stands for the initial mass fraction of the corresponding volatile species relative to the MO mass $M_{t=0}^{\text{MO}}$ at time $t = 0$.

We assume that the planetary mantle is oxidized (Gaillard et al., 2021). So, our coupled model considers three different volatile species: $H_2O$ that can condense in the atmosphere, $CO_2$ that cannot condense, and $N_2$ as a background atmospheric gas whose atmospheric abundance is set to be constant throughout the whole thermal evolution. The principle of hydrostatic equilibrium for the atmosphere states that the pressure at any point in a fluid at rest is due to the weight of the overlying fluid (e.g., Pierrehumbert, 2010). Hence, the total atmospheric pressure exerted over the planetary surface of an area $A = 4\pi R_p^2$ (where $R_p$ is the planetary radius), by the whole atmosphere, is related to its total mass following:

$$P_{\text{surf}} = \frac{g M_{\text{tot}}^{\text{atm}}}{A}. \tag{2}$$

As pointed out by B2019, considering that the atmosphere is made of a mixture of $k$ ideal gases, each individual gas species $i$ of partial pressure $P_i$ depends on the number of moles of each species $n_i$ according to the ideal gas law:

$$P_i V = n_i R T, \tag{3}$$

where $V$ is a local elementary volume of the gas mixture, $T$ is temperature, and $R \approx 8.314$ J.K$^{-1}$.mol$^{-1}$ is the perfect gas constant. Knowing the total pressure in this local elementary volume, $P$, makes it possible to calculate the molar fraction, $x_i = P_i/P$. Note that here, $P$ is different from the total surface pressure $P_{surf}$ defined above.

The hydrostatic relation permits to determine the total mass of the atmosphere from the total atmospheric pressure at the surface (Equation 2). One can of course rewrite locally, for an elementary volume $V$, the perfect gas

law (Equation 3) in terms of the mass of the specific gas $M_i^{\text{atm}}$ as follows: $P_i V = RT M_i^{\text{atm}}/\mu_i$ where $\mu_i$ is the molar mass of species $i$.

By definition of the mean molar mass:

$$\bar{\mu} = \sum_i x_i \mu_i = \sum_i \frac{P_i}{P} \mu_i, \tag{4}$$

At the surface,

$$\bar{\mu} = \sum_i \frac{P_{i,surf}}{P_{surf}} \mu_i, \tag{5}$$

Considering that the atmosphere is a mixture of perfect gases of mean molar mass $\bar{\mu}$, It is then straightforward to obtain (e.g., Pierrehumbert, 2010):

$$M_i^{\text{atm}} = \frac{4\pi R_p^2}{g} \left( \frac{\mu_i}{\bar{\mu}} \right) P_{i,surf}, \tag{6}$$

Here, we suppose that the atmosphere is only constituted of gases to determine the mass of each volatile degassed into the atmosphere that satisfies the mass balance Equation 1. Those surface pressures are then used by the atmospheric model that calculates the pressure and thermal profile in the atmosphere with:

$\mu_{H_2O} = 18\ \text{g}.mol^{-1}$, $\mu_{CO_2} = 44\ \text{g}.mol^{-1}$, and $\mu_{N_2} = 28\ \text{g}.mol^{-1}$.

Equation 6 is now used in our model to relate the mass of each volatile species, $i$, in the atmosphere, $M_i^{\text{atm}}$, to its partial pressure $P_{i,surf}$ at the surface. Note that for each component, the atmospheric partial pressure $P_{i,surf}\left(X_i^{\text{liquid}}\right)$ corresponds to the saturation pressure of the volatile in the melt and is thus a function of the corresponding volatile mass fraction in the liquid $X_i^{\text{liquid}}$ calculated from the interior model at each time step.

We assume efficient outgassing: as soon as the concentration of each volatile species in the melt $X_i^{\text{liquid}}$ exceeds its saturation limit (Equations C3 and C4 in S2017), the volatile species exsolve out of the melt to form gas bubbles. Those bubbles rise and burst out at the surface fast enough not to be carried back downwards within the convective flow. Thus, all volatile species in excess of saturation are expelled out into the atmosphere at each time step. Recent work considering bubbles as passive tracers suggests that very turbulent convection could delay the process, although by an amount that remains small compared to the duration of the MO phase (Salvador & Samuel, 2023). On the other hand, when the density difference between bubbles and melt is considered, quasi-immediate expulsion of the bubbles in the atmosphere appears to be valid (Patocka et al., 2020, 2022).

Omitting the molar masses ratio $\mu_i/\bar{\mu}$ in Equation 6 would be correct for single-component atmospheres only. Thus, the atmospheric pressures formerly expressed in S2017 do not correspond to atmospheric partial pressures but instead should each be understood as the equivalent atmospheric pressure of a given volatile species if this species was fully outgassed and considered to be alone in the atmosphere.

The calculation of the other terms in Equation 1 remains the same as in S2017, that is, the mass of each volatile species in the crystallizing mantle $M_i^{\text{solid}}$ writes:

$$M_i^{\text{solid}} = k_i X_i^{\text{liquid}} M_{\text{solid}}, \tag{7}$$

where the partitioning of volatile $i$ between the melt and the solid phase is controlled by the partition coefficient $k_i$ which determines how much of the volatile liquid mass fraction $X_i^{\text{liquid}}$ is stored in the solid mantle of mass $M_{\text{solid}}$. The mass of each volatile species within the molten phase $M_i^{\text{liquid}}$ writes:

$$M_i^{\text{liquid}} = X_i^{\text{liquid}} M_{\text{liquid}}, \tag{8}$$

and corresponds to the volatile mass fraction $X_i^{\text{liquid}}$ relative to the mass of the molten phase $M_{\text{liquid}}$.

For the multi-components system considered in our model, simultaneous degassing of both $H_2O$ and $CO_2$ implies an interdependence between the mass of the two volatile species in the atmosphere at each time step (after Equations 5 and 6):

$$\begin{cases} M^{\text{atm}}_{\text{H}_2\text{O}} = \dfrac{4\pi R_p^2}{g}\left[\mu_{\text{H}_2\text{O}}\left(\dfrac{\mu_{\text{H}_2\text{O}}P_{\text{H}_2\text{O}} + \mu_{\text{CO}_2}P_{\text{CO}_2} + \mu_{\text{N}_2}P_{\text{N}_2}}{\left(P_{\text{H}_2\text{O}} + P_{\text{CO}_2} + P_{\text{N}_2}\right)}\right)^{-1}\right]P_{\text{H}_2\text{O}}, \\ M^{\text{atm}}_{\text{CO}_2} = \dfrac{4\pi R_p^2}{g}\left[\mu_{\text{CO}_2}\left(\dfrac{\mu_{\text{H}_2\text{O}}P_{\text{H}_2\text{O}} + \mu_{\text{CO}_2}P_{\text{CO}_2} + \mu_{\text{N}_2}P_{\text{N}_2}}{\left(P_{\text{H}_2\text{O}} + P_{\text{CO}_2} + P_{\text{N}_2}\right)}\right)^{-1}\right]P_{\text{CO}_2} \end{cases}, \tag{9}$$

where the partial pressures of both $H_2O$ and $CO_2$ volatile species at the surface, are calculated from their mass fraction in the melt as an output of the interior model $\left(P_{i,surf}\left(X_i^{\text{liquid}}\right)\right)$. The corrected volatile mass balance implies solving numerically the system of two coupled nonlinear Equation 9 to determine $P_{\text{H}_2\text{O}}$ and $P_{\text{CO}_2}$ at each time step using a Newton-Raphson iterative method.

### 2.2. Summary of the Coupled Model

The rest of the coupled model is unchanged compared to S2017, and we are just summarizing here the main steps.

Besides the mass conservation, we solve the conservation of energy in the solidifying MO, which balances the mantle secular cooling with the heat sources: at the surface due to convection $F_{conv}$, at the Core-Mantle boundary $F_b$, due to internal heating by radioactive decay $H_{int}$, and due to the latent heat of solidification $H_{sol}$:

$$\int_{R_B}^{R_P} \rho C_p \frac{dT(r)}{dt} r^2 dr = R_P^2 F_{conv} + R_B^2 F_b + H_{int} + H_{sol} \tag{10}$$

where $\rho$ is the averaged density of melt and solid, $C_p$ the specific heat, $T$ the radial potential temperature, $r$ the planetary radius variable and $t$ is time. $R_P$ and $R_b$ stand for the planetocentric altitude of the spherical planet surface and that of the base of the MO, respectively. $F_b$ is negligible compared to $F_{conv}$. The latter depends on the intensity of convection in the MO and writes

$$F_{conv} = C_0 k \frac{T_m - T_{surf}}{R_P - R_b} Ra(R_P - R_b, T_m - T_{surf})^{1/3} \tag{11}$$

$C_0$ is a constant which depends on the pattern of convection. The Rayleigh number depends on the temperature difference between the potential temperature of the bulk mantle $T_m$ and the upper surface temperature $T_{surf}$, and the viscosity at the mantle potential temperature $\nu_m$:

$$Ra(R_P - R_b, T_m - T_{surf}) = \frac{\alpha g (T_m - T_{surf})(R_P - R_b)^3}{\kappa \nu_m} \tag{12}$$

where $\kappa$ is the thermal diffusivity, $k$ is the thermal conductivity, and $\alpha$ is the thermal expansion coefficient. We assume that Equations 11 and 12 are valid during the whole history of the MO, even after the rheological transition has been reached. Although a more viscous thermal boundary layer can develop at the surface, this hypothesis implies that it does not remain stagnant but that it can break and sink back episodically in the mantle, due for example to impacts, faulting due to rapid thermal contraction, or an early plate tectonic regime. This strong hypothesis will be further discussed in Section 4.1.

The secular term (left-hand side of Equation 10) is integrated over the whole mantle, which means that cooling due to any convective instability coming from the upper surface is redistributed over the whole mantle, either through turbulent convection in the liquid, porous flow inside the mush, or convective overturn inside the growing solid-state mantle (see discussions in Lebrun et al. (2013) and S2017).

Then, degassing makes the atmosphere grow. The atmosphere is in turn heated both by the incoming solar flux and by the heat flux coming from the solidifying MO. As in S2017, the atmospheric part of the model uses the code RADCONV1D described in Marcq et al. (2017). It is a radiative-convective model which can run

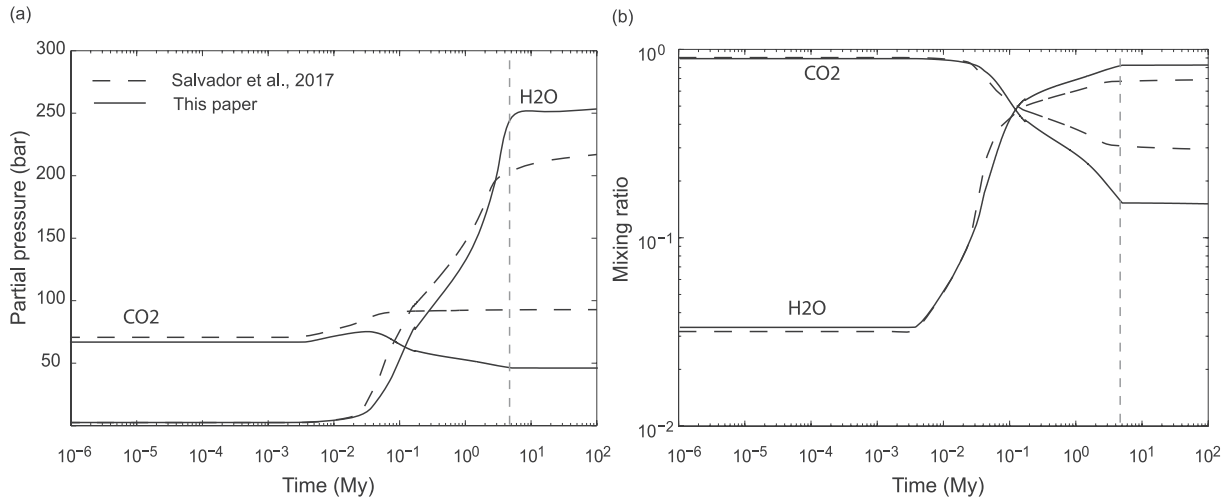


**Figure 1.** Volatile outgassing history ($H_2O$ and $CO_2$) considering the corrected (plain lines) and incorrect (dashed lines) volatile mass balance, with initial volatile mantle abundance $X_{H_2O,t=0} = 410$ ppm and $X_{CO_2,t=0} = 130$ ppm (similar to Reference-A model of Nikolaou et al. (2019)), for a planet orbiting the young Sun at $D = 1{\cdot}$AU, an albedo equals to 0.3 and the current solar constant of 340 W m$^{-2}$. (a) Outgassed volatile partial pressures and (b) corresponding mixing ratios (molar fraction) for both $H_2O$ and $CO_2$. End of the Rapid Cooling Stage is indicated by the dotted vertical line. See Massol et al. (2023b) for data.

considering either gray emission or *k*-correlated emission (hereafter referred to as "non-gray"). Atmospheric escape is neglected.

We consider an Earth-size planet and a mantle with a chondritic composition. The initial potential temperature of the MO is 4000 K, whereby the mantle is entirely molten. We assume that solidification develops from the bottom. The early solar constant is calculated from the estimates of the Sun's radius and effective temperature given in Tables 1 and 3 of Bahcall et al. (2001). At the 1 AU Earth's location, it gives a value of 925 W m$^{-2}$, slightly below our previous estimate of 970 W m$^{-2}$ (S2017, after Gough, 1981).

We define the End of the Rapid Cooling Stage (ERCS) as the time when the interior heat flux ($F_{conv}$) becomes negligible compared to the absorbed solar flux ($F_{\odot}$), that is, $F_{conv} \leq 0.1 \times F_{\odot}$. This criterium based on a heat flux balance allows to compare planets that will remain molten with planets that solidify, something that a criteria based on melt content cannot do.

## 3. Results

### 3.1. Thermal Evolution for Different Solar Distances

Figure 1 illustrates the changes in the evolution of the atmospheric pressure. Here, we use a prescribed albedo of 0.3 to compare our results with recent papers (Bower et al., 2019; Nikolaou et al., 2019). Because $CO_2$ is less soluble in magmas than $H_2O$, it is degassing first in the atmosphere. But once $H_2O$ reaches its solubility threshold and degasses also, the partial pressure of $CO_2$ decreases (Figure 1a): this is the main difference with our previous paper S2017. Moreover the mixing ratio of $H_2O$ increases and overcomes $CO_2$'s (Figure 1b) more drastically than in S2017. As both $CO_2$ and $H_2O$ are greenhouse gases, a change in their partial pressure also affects the thermal blanketing of the atmosphere, and thus the surface temperature, which in turn affects the thermal evolution of the MO. Since $H_2O$ radiative forcing is higher than that of $CO_2$, decreasing the $CO_2$ atmospheric pressure relatively to that of $H_2O$ implies that the opacity of the atmosphere increases, so that the thermal blanketing effect is more efficient (Section 3.2 of S2017). Heat is then evacuated less efficiently through the opaque atmosphere. Thus, if water condensation does not occur at the surface (i.e., for planets located inside the critical distance), the higher $H_2O$ partial pressure (Figure 2e) implies a higher surface temperature at ERCS ($\Delta T = +140$ K, i.e., 9% difference, Figure 2a) and it takes more time to reach ERCS (ERCS is reached at 0.09 Myr i.e., 16.4% later, for planets located at $D = 0.77$ AU, Figure 2). However, for planets located beyond the critical distance, where water condensation occurs on the surface, ERCS is reached earlier than in S2017, at 1.4 Myr instead of 2 Myr. This is because more $H_2O$ is trapped into the water ocean

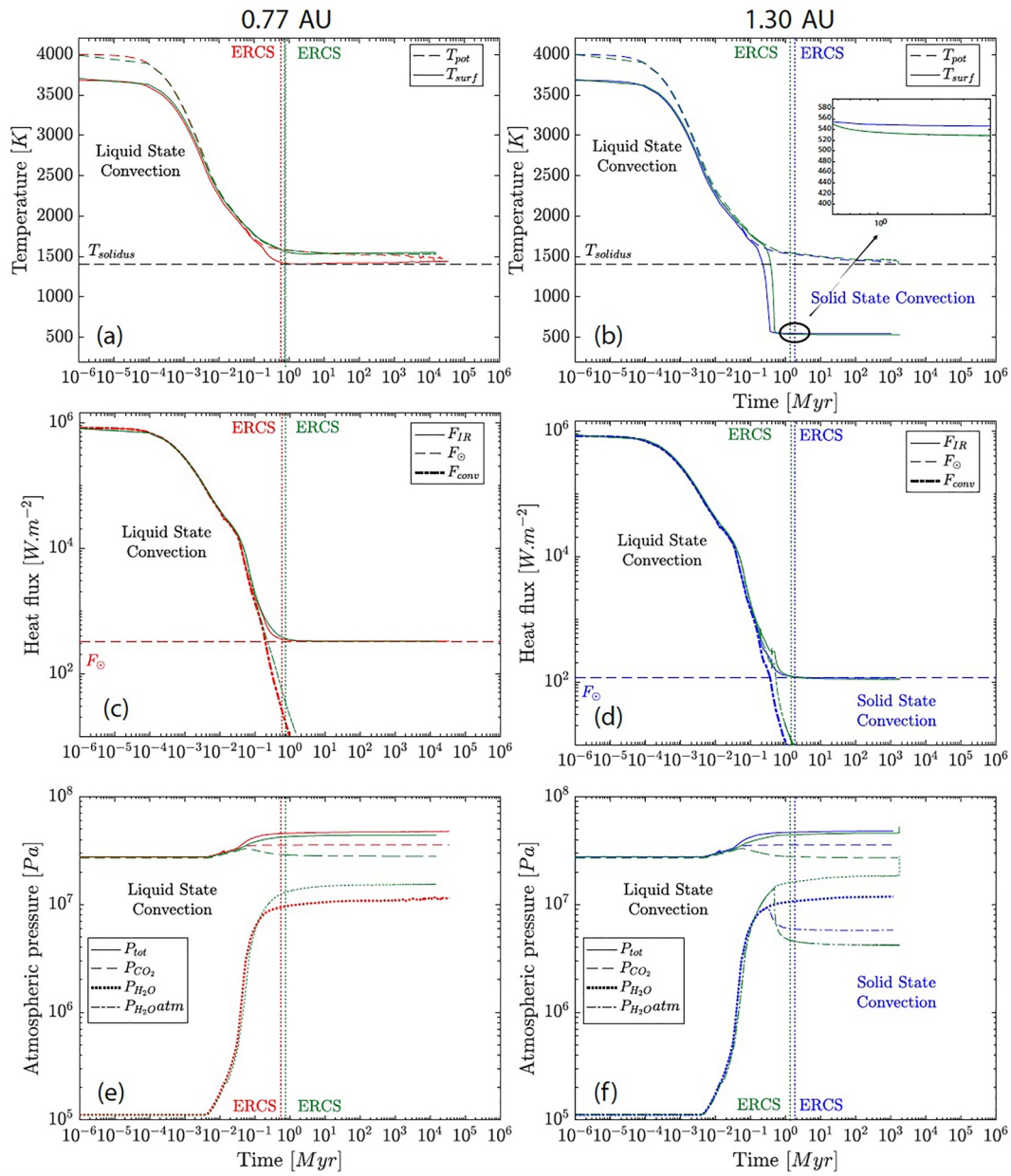


**Figure 2.** Update of Figure 5 of S2017: Thermal evolution of the Magma Ocean for two different distances from the Sun: 0.77 AU (a, c, and e) and 1.30 AU (b, d, and f). Blue and red curves stand for the previous incorrect data, and green curves are the corresponding corrected data. Note that when no condensation occurs at the surface End of the Rapid Cooling Stage is delayed whereas it is the opposite when condensation occurs. In the $D = 0.77$ AU case, the calculation is stopped before the surface is totally solid. Indeed because the planet is within the critical distance from the sun, and no gas escape is considered in our model, the surface stays molten (≈25% melt). In the $D = 1.3$ AU case, the calculation stops when the solidification is complete. See Massol et al. (2023b) for data.

and the atmospheric partial pressures at ERCS are lower than in our previous estimates (Figure 2f). The resulting surface temperature at ERCS is therefore slightly lower ($\Delta T = -17.7$ K, i.e., 3.2% difference with S2017, Figure 2b and figure inset).

The difference in the thermal evolution and resulting surface conditions between our previous results and the ones obtained with the corrected volatile mass balance are then logically explained by the influence of the relative $H_2O$-$CO_2$ contents of the atmosphere at ERCS.

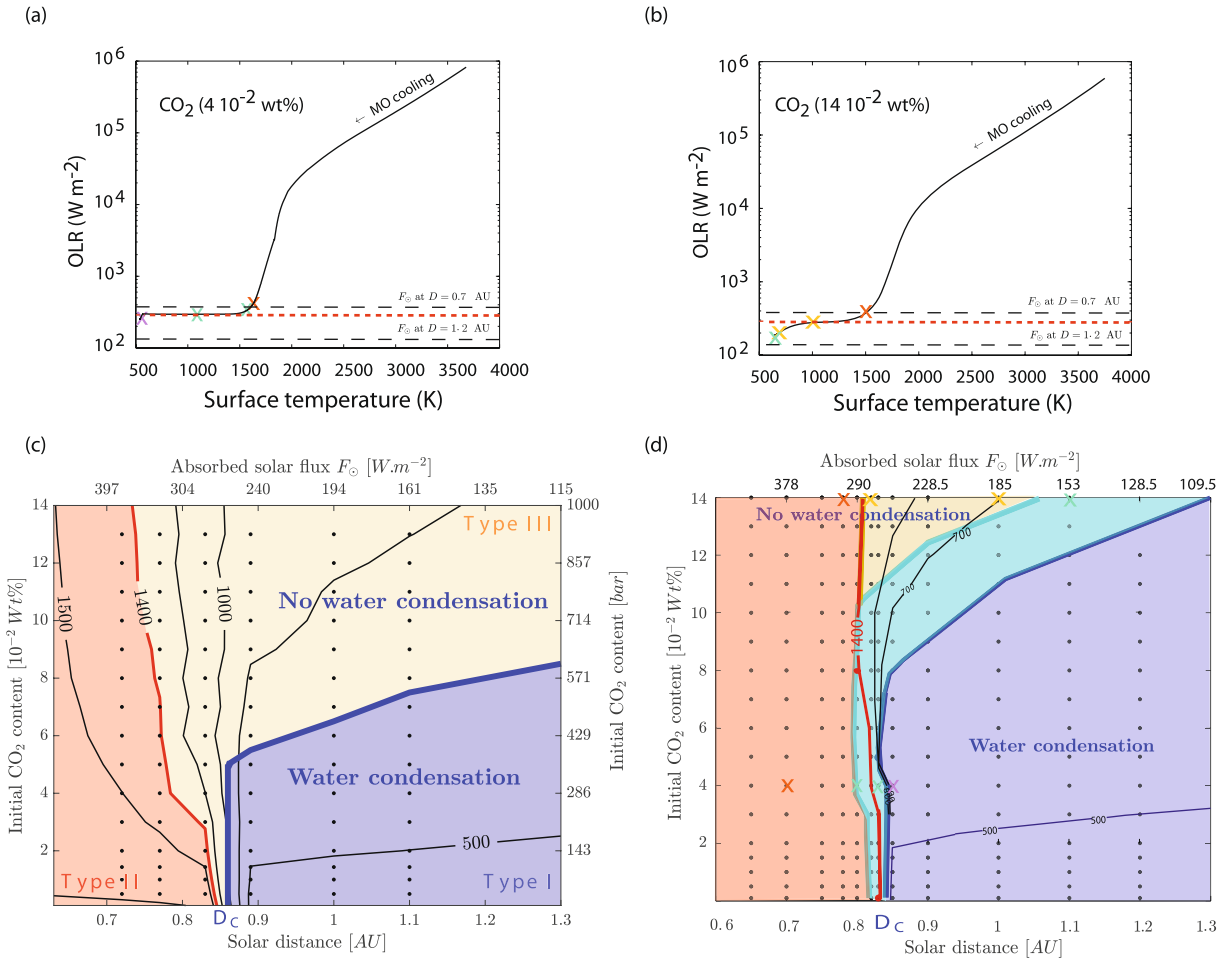


**Figure 3.** (a and b) Outgoing thermal flux as a function of temperature for (a) $H_2O$-dominated $\left(X_{CO_2,t=0} = 4 \times 10^{-2}\ wt\%\right)$ and (b) $CO_2$-dominated atmospheres $\left(X_{CO_2,t=0} = 14 \times 10^{-2}\ wt\%\right)$. Horizontal top and bottom black dashed lines indicate the solar flux absorbed by a planet located at $D = 0.7$ AU and $D = 1.30$ AU, respectively. The horizontal red dotted line indicates the radiation limit of a steam atmosphere, Simpson-Nakajima limit (280 W.m$^{-2}$). The colored "$x$" indicates the surface conditions reached at End of the Rapid Cooling Stage (ERCS) for type I (blue), type II (red), type III (yellow) planets and planets that condense water later than ERCS (green) corresponding to the "$x$" shown in (d). (c) Figure 7 from S2017 (d) Update of Figure 7 of S2017: Influence of the solar distance and $CO_2$ initial content on the surface conditions reached at ERCS for an initial $H_2O$ content of ~0.6 Earth ocean mass. Blue, yellow, and red shaded areas indicate the three types of planets reached at ERCS. The green area shows the conditions for which a planet will not have yet condensed water at ERCS but will condense water later in its history. The black contour lines display the temperature contour at ERCS. See Massol et al. (2023b) for data.

### 3.2. Influence of the Initial $CO_2$ Content

The existence of three types of planets at ERCS (Figure 3) remains valid, depending on the initial $H_2O$ and $CO_2$ contents and the distance to the star:

- Close to the star, a planet with a molten surface and therefore no water ocean (type II of Hamano et al. (2013))
- Beyond a critical distance to the star and for low enough initial $CO_2$ content, a planet with a surface cold enough to condensate a water ocean (type I of Hamano et al. (2013))
- Beyond a critical distance to the star and for high enough initial $CO_2$ content to prevent water condensation, a planet with a solid surface but no water ocean (type III of S2017). This last planetary type could not be observed in Hamano et al. (2013) since only $H_2O$ was initially present in their MO.

The limits between the three regimes are modified by the correction (Figure 3).

As discussed in the previous section, when no water ocean is formed (type II planet), higher $H_2O$ and lower $CO_2$ atmospheric partial pressures increase the greenhouse effect of the atmosphere and it results in higher surface

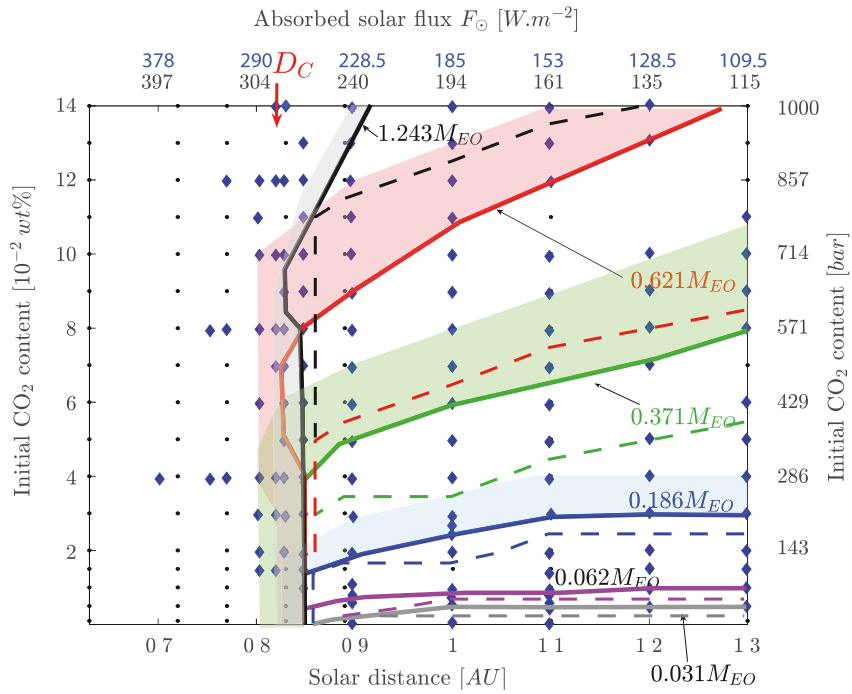


**Figure 4.** Update of Figure 10 of S2017: S2017 (dashed lines) and updated (solid lines) water condensation limits at End of the Rapid Cooling Stage (ERCS) on an Earth-like planet for different water contents. The shaded areas above each solid line represent parameter domains where water ocean condensation has not yet happened at ERCS but happens later in the planet's evolution. Above these condensation limits water condensation does never occur, while below the solid lines, a water ocean is always present at ERCS. Note that the domain where condensation can occur is expanding as initial water content increases. Blue diamonds show the calculation points in the present corrected paper, while black dots represent S2017 calculation points. The critical distance $D_C$ does not vary much between S2017 and the corrected model. See Massol et al. (2023b) for data.

temperatures at ERCS (between 4.5% and 9% temperature difference at 0.77 AU for initial $CO_2$ contents of $10^{-2}$ and $10^{-1}$ wt%, respectively; see the plain line corrected isotherms of Figure 3d).

Beyond the critical distance, higher $H_2O$ partial pressures favor the formation of water oceans (type I planet). However, when increasing the $CO_2$ content, the OLR (Outgoing Longwave Radiation) deviates from the water vapor atmosphere behavior as can be seen in Figures 3a and 3b: Figure 3b displays a shorter plateau at the Nakajima limit flux value than Figure 3a, as its $CO_2$ content is higher. For high enough $CO_2$ content, this will result in the absence of condensation of a water ocean, despite a solid planetary surface (type III planet). Compared to S2017, the water condensation limit at ERCS for a given initial water content is shifted to higher initial $CO_2$ contents (blue curve in Figure 3d). For instance, at $D = 1.00$ AU, the critical initial $CO_2$ content preventing water ocean formation is shifted from $6.5 \times 10^{-2}$ wt% (S2017) to $11.5 \times 10^{-2}$ wt% in the corrected case (76.9% difference). The parameter space where water condensation occurs at the planetary surface is extended, which increases the likelihood of early water ocean formation. Moreover, this water condensation zone is further extended when we consider the cases where a water ocean condensates later than ERCS in the planetary evolution (green area on Figure 3d).

### 3.3. Influence of $H_2O$ Content

Figure 4 shows that increasing the initial water content extends the $CO_2$ concentration range for which water condensation at the surface at ERCS is possible. To understand this trend which might seem counterintuitive considering the greenhouse effect described in Section 3.1, we plot the surface conditions at ERCS on the water phase diagram and the associated thermal atmospheric profiles (Figure 5).

In the framework of Marcq et al. (2017) model, the more there is water, the more it condenses in the atmosphere, thus lowering the surface temperature due to the milder slope of the wet adiabats. Our modeling does not consider the increase of the albedo due to cloud formation, but the latter will tend to lower even more the surface temperature, so our interpretation should remain valid. So, beyond the critical distance $D_C$ and within

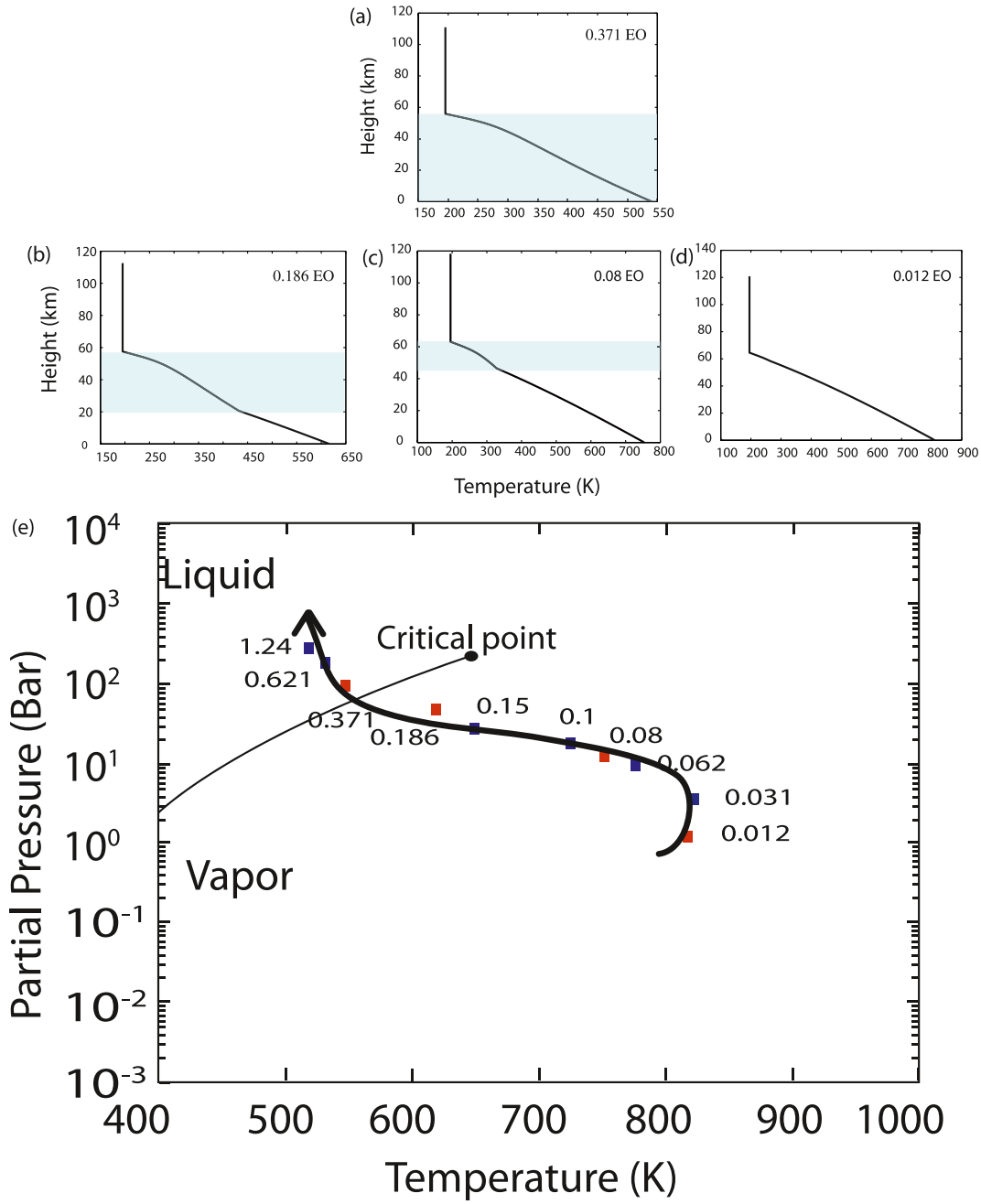


**Figure 5.** Water phase diagram and surface conditions at End of the Rapid Cooling Stage for an initial $CO_2$ content of $4 \times 10^{-2}$ wt% in the case of Earth ($D = 1$ AU). The red squares on (e) indicate conditions for which we plot the atmospheric temperature profiles (a–d). The numbers on the thick black curve of (e) are the water contents initially dissolved in the Magma Ocean. The light blue zones drawn in the atmospheric profiles (a–d) show the part of the atmosphere where condensation occurs. For water content greater than 0.35 here, this zone extends to the surface to form a water ocean. See Massol et al. (2023b) for data.

the water condensation area (blue area in Figure 3c), the higher atmospheric $H_2O$ partial pressures obtained as solidification proceeds imply a larger amount of water condensed in the oceans. These oceans are therefore deeper at ERCS than in S2017. As more water is trapped within the oceans, the $H_2O$ atmospheric concentration decreases; this reduces the greenhouse effect of the atmosphere, and the surface temperatures at ERCS are therefore lower in the condensed (blue) part of the diagram (see the plain line corrected isotherms of Figure 3d in comparison of the isotherms of Figure 3c).

**Table 1**
*Coefficients to Be Used in Equation 16 to Draw the Condensation Limits Separating Planets Where Water Ocean Formation Occurs or Not at End of the Rapid Cooling Stage Shown in Figure 6*

| Rad. transfer | Prefactor $a$ | Exponent $n$ |
|---|---|---|
| Incorrect volatile mass balance—Salvador et al. (2017) | | |
| Gray | 0.82 | 0.05 |
| $k$-correlated | 0.902 | 0.128 |
| Corrected volatile mass balance | | |
| Gray | 0.88 | 0.03 |
| $k$-correlated | 0.94 | 0.09 |

Note that the critical distance $D_C$ separating the types I and II planets does not appear to be much affected by the correction (Figures 3 and 4).

### 3.4. Scaling Law for the Water Condensation Limit

As already noted by S2017, all the curves limiting the condensation domain have similar shapes and we therefore can look for a scaling law to collapse all the data. We can define a dimensionless number $X^*$ representative of the relative abundance of greenhouse gases $H_2O$ and $CO_2$ in the atmosphere. To avoid any possible confusion between equivalent atmospheric pressures formerly calculated in S2017 and corrected atmospheric partial pressures, this dimensionless parameter is now expressed in terms of volatile mass fractions initially dissolved within the MO $X_{i,t=0}$:

$$X^* = \frac{X_{CO_2,t=0}}{X_{CO_2,t=0} + X_{H_2O,t=0}}. \tag{13}$$

Since for a single species in the atmosphere, $P_{i,surf}$ and $X_{i,t=0}$ are proportional, $X^*$ is equivalent to the dimensionless number based on the pressures used in S2017, so that we can compare with our previous paper (Equation 11 in S2017). As previously mentioned, this scaling is based on the initial volatile content of the MO without anticipating on the results. Following S2017, the dimensionless distance to the star $D^*$ is defined as:

$$D^* = \frac{D}{D_C}, \tag{14}$$

where the critical distance $D_C$ (in AU) in a given stellar system of the solar constant defined at Earth distance from the star $\mathcal{F}'_0$ and for a given planetary albedo $\alpha$ writes:

$$D_C = \sqrt{\frac{\mathcal{F}'_0(1-\alpha)}{OLR_N}}, \tag{15}$$

where $OLR_N$ is the radiation limit of steam atmospheres shown in Figures 3a and 3b, $OLR_N = 280$ W m$^{-2}$ (Marcq et al., 2017). This is the same scaling as already tested by Hamano et al. (2013, 2015) and Kopparapu et al. (2013) for an albedo equal to 0.3. But we extend its validation for albedos between 0.1 and 0.8.

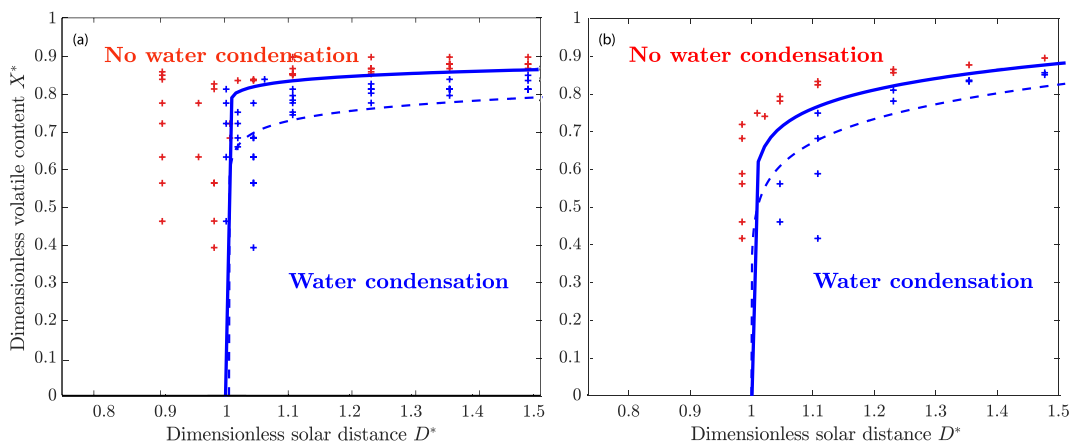


**Figure 6.** Update of Figure 12 of Salvador et al. (2017): Previous (dashed lines) and updated (plain lines) Earth-like planets' water condensation limits at End of the Rapid Cooling Stage as a function of the dimensionless initial volatile content $X^*$ and the dimensionless stellar distance $D^*$, for (a) a gray radiative-convective and (b) a non-gray $k$-correlated atmospheric model approximation. Those limits have been drawn by fitting data obtained for different $H_2O$ contents (crosses) using Equation 16 and corresponding coefficients of Table 1 (see also Massol et al. (2023b) for data).

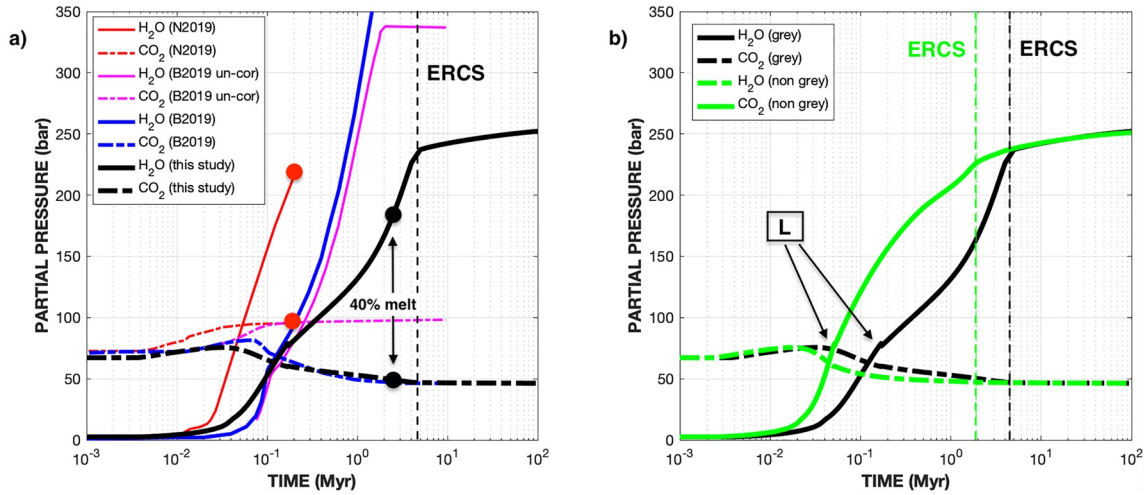


**Figure 7.** Comparison of the evolution of $H_2O$ and $CO_2$ outgassing pressures for different models with initial volatile mantle abundance $X_{H_2O} = 410$ ppm and $X_{CO_2} = 130$ ppm (similar to Reference-A model of Nikolaou et al. (2019)), for a planet orbiting the young Sun at 1 AU. (a) Comparison of our corrected model (in black) with the uncorrected model of N2019 (in red), the uncorrected (in magenta), and the corrected (in blue) models of B2019. N2019 model was stopped when 40% melt was obtained (red circles), while the other models were continued until melt disappearance. Our End of the Rapid Cooling Stage (ERCS) time is indicated by the dashed gray vertical line. The melt fraction at ERCS was 25% and the 40% melt fraction was reached after 2.5 Myr. All 4 models use gray radiation. (b) Comparison between our gray (in black) and non-gray *k*-correlated (in green) models for the same initial parameters as (a). The change of slope (indicated by "*L*") in the degassing path is due to the two orders of magnitude difference in the partition coefficients between Lherzolite for the upper mantle and perovskite for the lower mantle. See also Massol et al. (2023b) for data from our model.

Using $X^*$ and $D^*$ permits to get a single master curve delimiting the parameters domain where water ocean condensation occurs. The equation of this master curve associated with the critical dimensionless initial volatile content $X_C^*$ writes:

$$X_C^* = a \times (D^* - 1)^n, \tag{16}$$

where prefactor $a$ and exponent $n$ are given in Table 1. The corrected condensation limits are shown in Figure 6 (solid lines) along with the former limits based on an incorrect volatile mass balance (dashed lines), for both gray (Figure 6a) and non-gray *k*-correlated (Figure 6b) atmospheric radiative transfer approximations. The correction results in an average $X_C^*$ increase of 7.1% for the condensation limits obtained with the gray atmosphere (Figure 6a), and 12.9% for the non-gray atmosphere where the radiative transfer is more realistic (Figure 6b). The scaling law 16 is valid only for $CO_2$—$H_2O$ atmospheres and also depends on the assumptions used for both the MO and atmospheric models. For example, (Marcq et al., 2017) assumes that the condensed species in the atmosphere is not retained in the atmosphere as in Kasting (1988). Recent atmospheric models such as Graham et al. (2021) make other assumptions for the moist troposphere which should influence Equation 16.

## 4. Discussion

### 4.1. Comparison With Recent 1D Models: Time Evolution of the Coupled Mantle-Atmosphere System

Figure 7 compares our results in gray and in non-gray (same parameters used as in Figure 1) with two recent 1D MO-atmosphere coupled models (Bower et al., 2019; Nikolaou et al., 2019). Calculations were conducted using the same initial conditions (e.g., same constant albedo and same initial volatile content), but the temporal evolutions show some systematic differences that come from the different hypotheses adopted in each model. Figure 8a shows the solidus and liquidus curves used by the different models.

First of all, note that N2019 use an uncorrected version of the volatile mass balance and therefore should be best compared with the uncorrected version of B2019. Moreover, N2019 stop their calculation when the rheological transition (i.e., 40% melt) reaches the surface, while the other models pursue the calculation up to the complete solidification of the MO. The modelization adopted for the MO is the same for N2019 and our model (Section 2.2), while B2019 use mixing length theory (Spiegel, 1963). However, for this comparison, B2019 use a constant mixing length, that leads to a surface heat flux of the same form as Equation 11. Besides, B2019 remove

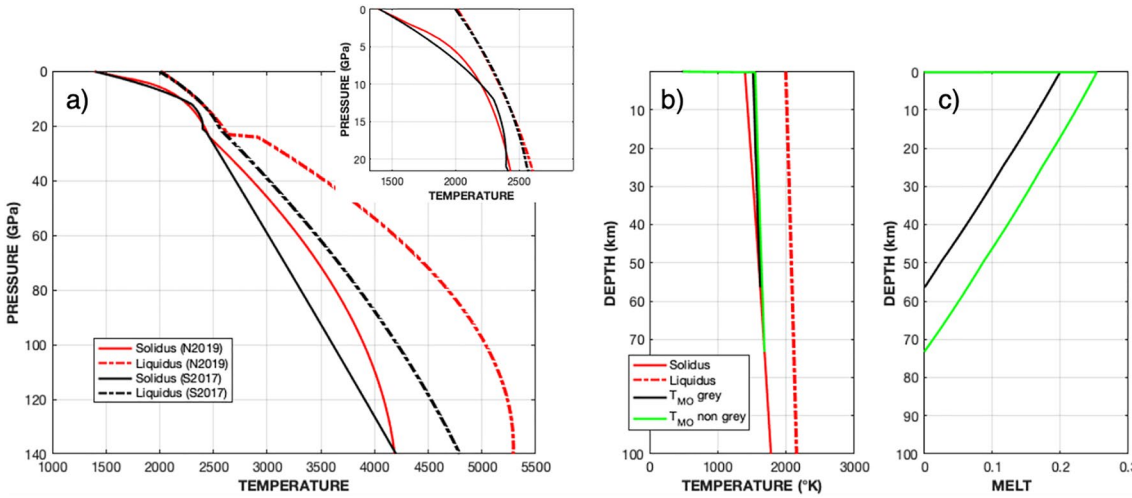


**Figure 8.** (a) Liquidus and solidus used by S2017 (in black; after Andrault et al., 2011), and by N2019 (in red). The insert focuses in the upper mantle. B2019 took profiles similar to N2019 for the upper mantle, and similar to S2017 for the lower mantle. (b) S2017 liquidus and solidus as well as the potential temperature at End of the Rapid Cooling Stage as a function of depth for the gray (in black) and non-gray (in green) runs of Figure 7. The thickness of the surface thermal boundary layer is 185 and 181 m, respectively. (c) corresponding melt distribution below the surface.

the thin thermal boundary layer at the top of their MO model, which ensures that all the volatiles are degassed. Both N2019 and B2019 implemented a gray radiative atmosphere, while we implemented a radiative-convective atmosphere, with either gray or *k*-correlated radiation (S2017).

All models show the same early degassing of $CO_2$, with two types of time evolution, with eventually decreasing partial pressures for the corrected models, and constant partial pressures for the uncorrected models, as already discussed in Section 3.1. $H_2O$ degassing starts earlier (by a factor of at least 2) in N2019 than in the other models. This is not due to the uncorrected version of the volatiles mass balance since $H_2O$ degassing starts at about the same time in the corrected and uncorrected versions of B2019. The discrepancy is instead probably due to the different solidus and liquidus curves adopted for the lower mantle (Figure 8a): the synthetic KLB-1 peridotite curves taken by N2019, with much higher liquidus temperatures than the chondritic liquidus taken by B2019 and S2017, imply that solidification is beginning earlier in N2019, therefore concentrating $H_2O$ in the melt and producing its outgassing in the atmosphere earlier. Then the $H_2O$ degassing rate is higher in N2019 and B2019 than in our model. One reason is the different atmosphere modeling, as a gray radiative atmosphere allows cooling more rapidly than a gray radiative-convective atmosphere (i.e., Lebrun et al., 2013). Another reason might be the higher solidus temperatures for the upper mantle adopted in N2019 and B2019, compared to S2017. As already pointed out by N2019, at least half of the MO history is dominated by solidification dynamics in the upper mantle, and higher solidus temperatures imply an earlier end of melting and end of degassing.

The last difference between B2019 and our model concerns the final $H_2O$ partial pressures: although Figure 6 of B2019 does not show the final value, it is greater than 350 bars and should be bound by a maximum of 380 bars, which would correspond to the total degassing of the water initially dissolved in the MO. Our value of ∼250 bars is significantly lower. This is not due to the atmospheric model as Figure 7b shows that a radiative-convective *k*-correlated model will generate earlier $H_2O$ outgassing and ERCS than in the gray case, but the same amount of degassing. Our lower value is instead due to the reduced cooling and degassing of the MO because of its temperature structure and the formation of a viscous thermal boundary layer under the surface (Figure 8b). We see that even at ERCS, there is still up to 20% of melt just under the surface thermal boundary layer for the gray case and 25% for the *k*-correlated case (Figure 8c). Although we do not have a completely stagnant lid as in some of B2019 cases when they consider a variable mixing length (see also Krissansen-Totton, Galloway, et al., 2021), our melt and water evolution is between their early outgassing cases (such as the one displayed on Figure 7a) and their extended outgassing cases (in the case of a stagnant lid).

Even larger amounts of volatiles could remain in the melt trapped in the residual mantle if melt drainage out of the freezing front was inefficient (Hier-Majumder & Hirschmann, 2017; Miyazaki & Korenaga, 2022) or if it is assumed that the growth of a stagnant lid would prevent degassing (Bower et al., 2022). Moreover, the

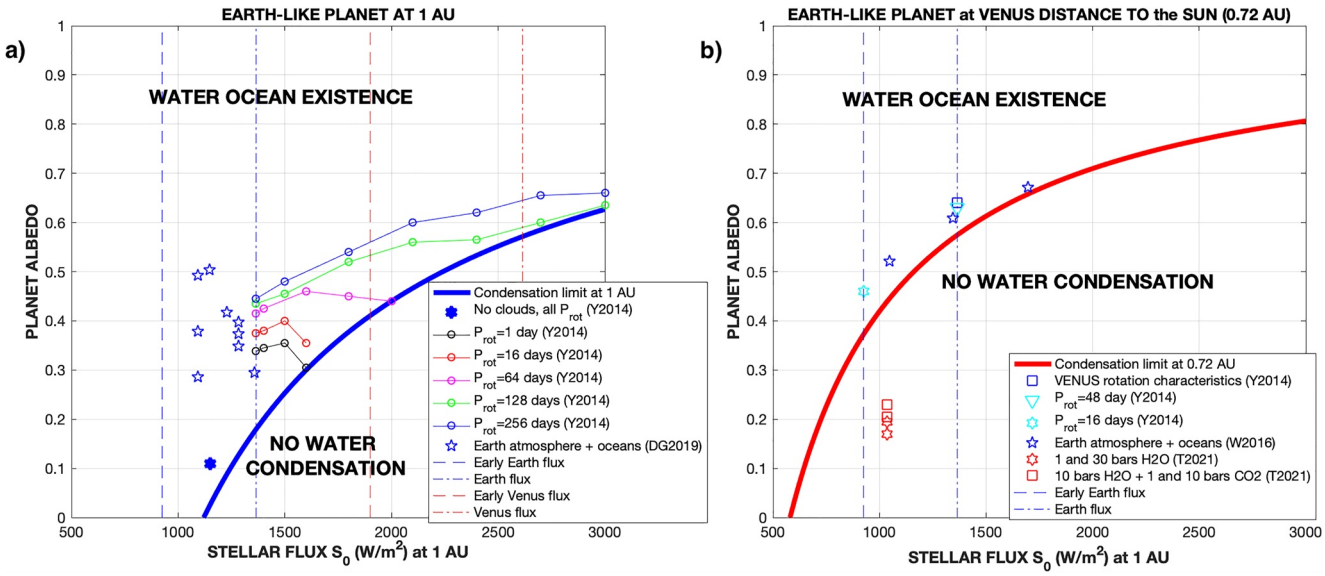


**Figure 9.** Condensation limit as a function of the stellar flux at 1 AU and the planetary albedo, calculated from Equation 16. (a) a planet like Earth (in terms of topography, water ocean, atmosphere) at 1 AU, with clouds for rotation periods $P_{rot}$ between 1 day and 256 days and increasing stellar fluxes (the color lines stop when the models diverge due to runaway greenhouse), and without clouds at all periods (Yang et al., 2014). The empty stars show an early Earth planet with different ages and atmospheric compositions (Del Genio et al., 2019). (b) a planet like Earth (e.g., already with a surface water ocean) at Venus distance from the Sun (0.72 AU) for different rotation rates (Yang et al., 2014), different stellar flux (Way et al., 2016), an Earth-size planet with clouds but no pre-existing liquid water on the surface (Turbet et al., 2021).

distribution of melt, and therefore of volatiles, in the mantle might not be uniform, depending on the volatiles extraction mechanism and the solubility laws. Besides into the asthenosphere, melt could also be trapped into the transition zone (e.g., Monteux et al., 2020), or at the bottom of the mantle (e.g., Labrosse et al., 2007; Miyazaki & Korenaga, 2022).

### 4.2. Comparison With 3D Atmospheric Models: Sustainability of a Water Ocean

1-D models do not allow to explicitly study clouds formation, even if attempts have been made to parameterized the effect of clouds on surface conditions (Forget & Pierrehumbert, 1997) and more recently, Koll (2022) or Windsor et al. (2023). However, the influence of the 3D distribution of clouds on the habitability of a planet cannot be accounted for by those 1D models.

In our model, we only considered the reflecting effect of water clouds through the albedo parameter and there was no retroaction between atmospheric volatile contents and albedo. We therefore ran our 1D models for a fixed value of the albedo over the whole MO history. And, as we showed in Section 3.4, the presence of a water ocean once the planet has solidified depends strongly on this albedo.

On the other hand, current 3D GCM are not coupled with interior dynamics, but they allow to investigate the influence of the 3D distribution of clouds on the existence of liquid water. The clouds distribution and the resulting planetary albedo depends in turn on the planet's rotation, the planet's topography, the atmosphere's volatile content and the incoming stellar flux. Most of the studies focused on the sustainability of an existing water ocean ("aqua" planet) or at least pockets of liquid water ("land" or "dry" planet) on the planetary surface (Abe et al., 2011; Leconte et al., 2013; Way & Del Genio, 2020; Way et al., 2016; Yang et al., 2014, 2019) as the solar flux increases. It is for slow planetary rotation that surface temperatures and a liquid water survive the longest to higher stellar fluxes (Figure 9): slow rotation favors the stability of clouds at the substellar point, resulting in high albedos. On the other hand, if water is under the vapor form in the atmosphere, clouds develop in the night side and the planetary albedo remains low: so the planet does never cool enough to condense water (Turbet et al., 2021). Although those two scenarios are very different, it is interesting to note that these 3D GCM still all plot in the corresponding parameter space delimited by the radiation limit of steam atmospheres (Equation 16) (see Figure 9).

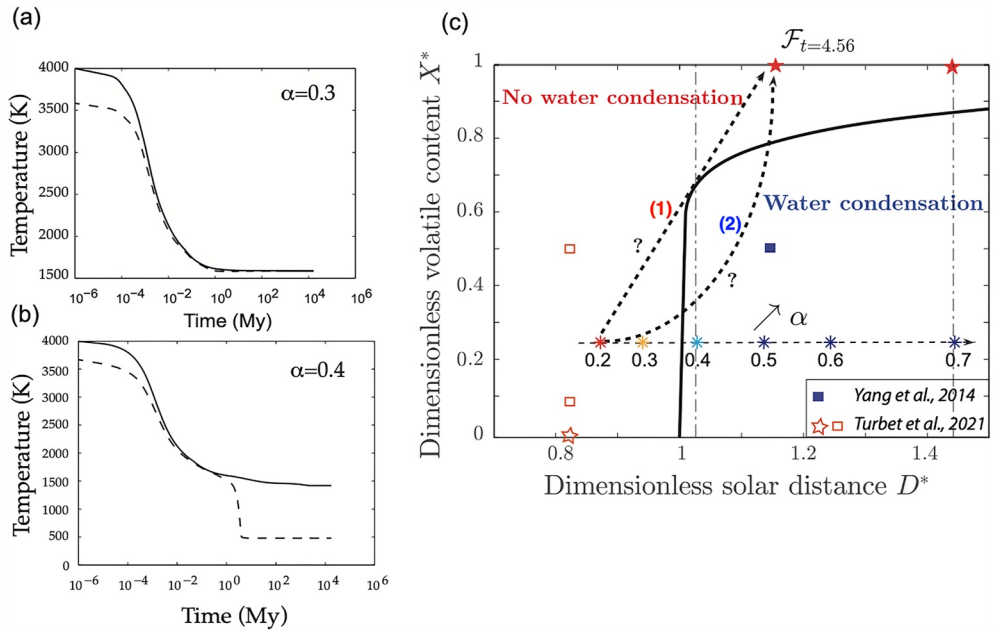


**Figure 10.** Scenarios for the early evolution of Venus. Dashed vertical lines represent $D^*$ for albedo 0.4 and 0.7 for Venus and early solar constant. The intersection with the curve allows determination of the minimum amount of water necessary to condense at the surface. 3D models by Yang et al. (2014) and Turbet et al. (2021) are represented by filled blue square and empty red squares and star, respectively. Red-filled stars represent the present-day atmosphere of Venus with $\mathcal{F}_{t=4.56}$ standing for the present-day solar flux. See text for explanations about the dashed curves (1) and (2). See Massol et al. (2023b) for data.

### 4.3. Implications for Venus Early Evolution

Some geochemical evidence suggest that Venus could have hosted on its surface more water in the past than today (Donahue et al., 1982; Krasnopolsky et al., 2013). Following Salvador et al. (2017), we can use our scaling laws (14)–(16) to evaluate different evolution scenarios for Venus. Due to the volatile mass balance correction, the shape of the condensation limits has slightly changed and extends water ocean formation to a larger $X^*$ (Figures 6a and 6b). Based on these updated curves, we can re-estimate the critical amount of water required to form a water ocean at the surface of early Venus, as a function of its albedo whose dependence is included in the dimensionless solar distance $D^*$.

For $H_2O$-dominated atmospheres, that is, $X^* < 0.5$, a critical albedo $\alpha_c = 0.38$ is sufficient to form a water ocean at Venus distance ($D = 0.72$ AU) for the flux emitted by the young Sun.

For $CO_2$-dominated atmospheres, that is, $X^* > 0.5$, early water ocean formation strongly depends on the relative volatile content. At Venus distance, and for an albedo $\alpha = 0.4$, $D^* = 1.02$ (vertical dotted line in Figure 10c). The corresponding critical dimensionless volatile content $X_C^*$ is given by Equation 16. Considering Venus' present-day $CO_2$ content (90 bar, converted in MO mass fraction $X_{CO_2,t=0}$ assuming it is the only and fully outgassed atmospheric species) in Equation 13, the corresponding minimal amount of water required to form an ocean is 0.13 Earth Ocean mass ($M_{EO}$), instead of 0.3 $M_{EO}$ in S2017, so that the formation of a water ocean is twice more likely in the corrected model compared to S2017.

On the other hand, with the observed volatile content in its present-day atmosphere (90 bars of $CO_2$, no water, albedo 0.7), Venus currently plots on $X^* = 1$ (indicated by the red-filled stars in Figure 10c). So there are two possible scenarios for Venus' evolution (Figure 10c): (1) either Venus never experienced liquid water on its surface; or (2) it had an initial volatile content and composition sufficient to condensate water early in its history. Modern constraints of a dense $CO_2$-dominated atmosphere with negligible water vapor and oxygen and reasonable abundances of outgassed $^{40}Ar$ and $^{4}He$ cannot discriminate between the two scenarios as both never-habitable and habitable histories could produce them (Avice et al., 2022; Gillmann et al., 2022; Krissansen-Totton, Fortney, & Nimmo, 2021).

Once Venus has a liquid water ocean, 3D GCMs show that it could survive even the present-day solar flux on Venus (Figure 9b), due to the slow rotation rate of the planet (Way & Del Genio, 2020; Way et al., 2016; Yang et al., 2014). Then, a dramatic event such as the simultaneous emplacement of several large traps on the surface has to be invoked to disrupt enough atmosphere dynamics to generate a run-away greenhouse, vaporize the oceans and release enough $CO_2$ to create present-day Venus (Way et al., 2016). But how does Venus get out of the MO stage with a liquid water ocean? This depends on its volatile content and on cloud albedo feedbacks. For rather low concentrations of vapor water and $CO_2$, GCMs show that clouds form on the night side of the planet, a moist greenhouse prevails and desiccation happens due to atmospheric escape (Turbet et al., 2021). This would tend to favor scenario (1). However, the volatile content remain rather small (between 1 and 30 bars for $H_2O$ and between 0 and 10 bars for $CO_2$) in those simulations compared to the current 90 bars of $CO_2$ and even 0.1 $M_{EO}$ water. And as one can note, the planetary albedo of Turbet et al. (2021) increases as the water vapor and $CO_2$ content increase (Figure 9b). This would suggest that for a sufficiently large amount of $CO_2$ and $H_2O$, Venus may have experienced a water ocean directly after the MO stage; which favor scenario (2). More GCMs need now to be run with higher volatile contents to confirm this.

### 4.4. Water Ocean Condensation in Exoplanets With $CO_2$/$H_2O$ Atmospheres

The diversity of exoplanets has been described in recent review papers (e.g., Wordsworth & Kreidberg, 2022) showing that those planets might be quite different from Earth, with for example, preserved massive atmosphere of $H_2$, leading to larger observed radius compared to their mass than for rocky planets. Indeed, recent measurements have shown that low-mass planets ($\approx$2 $M_\oplus$) have a hydrogen dominated envelopes indicating different accretion history than Earth (e.g., Owen et al., 2020). In this context, it is obvious that the model presented here might not be used as it is. This section hence does not intend to make an exhaustive or definitive assessment on the state of the surface of exoplanets but intend to extend the discussion toward this exciting field. Some ingredients are missing in our model if one wants to look in detail and exhaustively at exoplanets. For example, when looking at the evolution of close-in exoplanets, Schaefer et al. (2016) demonstrated the crucial impact of atmospheric escape (for a review on that process see Gronoff et al., 2020). The more massive atmosphere of those sub-neptune worlds should lead to deviation on greenhouse limits (e.g., Pierrehumbert, 2023). Also, the atmospheres of smaller rocky exoplanets may contain other volatile species than $H_2O$ or $CO_2$, leading to complex chemical reactions as a function of their abundance and temperature (e.g., Wordsworth & Kreidberg, 2022) thus influencing the inflection point of the runaway greenhouse (e.g., Boukrouche et al., 2021; Chaverot et al., 2022).

Nevertheless, in the framework of our assumptions, as already discussed (Sections 3.4 and 4.1), the results of other 1D models confirm the limits of habitability that we found as a function of the dimensionless solar distance and volatile content for $CO_2$-$H_2O$ atmospheres (Figure 11; N2019; Hamano et al., 2015; Lichtenberg et al., 2021). We can now use this regime diagram to infer the conditions of habitability for several exoplanets recently found (e.g., see Dorn and Lichtenberg (2021) for a recent compilation). As current observations do not allow to estimate the exoplanets albedo, we indicate a range of albedo between 0 and 0.7 for each exoplanet considered.

For instance, in the case of super Earth LHS 3844b (1.3 earth radii) orbiting a *M* dwarf ($T_{star}$ around 3100 K), it is plausible that the surface could have been melted if an atmosphere was present at ERCS because of the proximity of the planet from the star (on our dimensionless diagram, it would plot at a $D^*_{\alpha=0}$ distance of 0.1). However recent observations using the thermal phase curve, have shown a solid surface and the lack of an atmosphere (Meier et al., 2021). The temperature contrast between the substellar and antistellar point of $\approx$1000 K might even, according to the authors, trigger interior convection and original tectonic modes. It might indicate that planet is old, so that atmospheric escape may have taken place, thus desiccating the planet, and promoting with time solidification of the surface governed by the water loss rate as described in Hamano et al. (2013).

We also calculate the critical distance $D^*_{\alpha=0}$ for Kepler 36b of 0.06 confirming a plausible still melt interior (Dorn & Lichtenberg, 2021). Since its equilibrium temperature is $\approx$1000 K (Carter et al., 2012).

TOI1452b has a measured planetary mass (4.8 $\pm$ 1.3 Earth Mass) and an inferred bulk density of $5.6^{+1.6}_{-1.8}$ g cm$^3$, which is suggestive of a rocky core surrounded by a volatile-rich envelope with a water content of $22\%^{+21}_{-13}$ (Cadieux et al., 2022). Its position on our diagram $\left(D^*_{\alpha=0} = 0.64\right)$ suggests that at ERCS, liquid water could have existed on its surface only for rather high albedos ($\alpha > 0.6$) and for a $CO_2$ content such that $X^* < 0.6$. For a $CO_2$ content of 90 bars, condensation at the surface would thus required $\approx$0.22 $M_{EO}$.

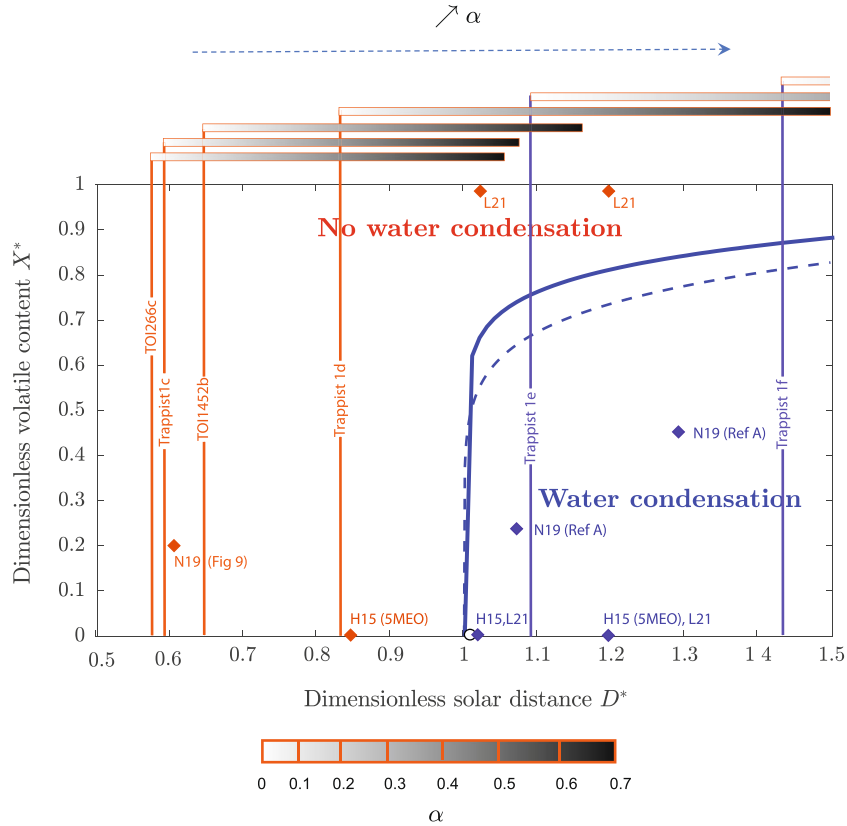


**Figure 11.** Habitability of exoplanets as a function of their volatile content and dimensionless solar distance, which depends on their albedo. Because their atmospheric composition is unknown we draw a vertical line at their dimensionless critical distance $D^*_{\alpha=0}$. Their albedo and the corresponding $D^*(\alpha)$ is color-coded in gray in the horizontal bars. We also indicated several 1D models by N2019, Hamano et al., 2015 (H2015) and Lichtenberg et al., 2021 (L2021). Red symbols indicate runs with no condensation; and blue symbols, runs with condensation of a water ocean.

The Trappist system consists in seven planets of the size of the Earth and of similar densities (Grimm et al., 2018). Their radius—mass relation suggests that they contain less than 0.1 wt% water distributed between mantle and surface (Dorn & Lichtenberg, 2021). Trappist-1c, like TOI 1266c, have a calculated critical distance $D^*_{\alpha=0}$ around 0.6, so that there was probably no chance to find water at the surface of these planets in their early history. Trappist-1d (Figure 11) is in a position comparable to early Venus (Figure 10c) and therefore the discussion of the previous section applies. Concerning Trappist-1e and 1f, our diagram confirms that a water ocean could have formed. If we suppose again the same value of 90 bar of $CO_2$ in their atmosphere, the minimum water contents necessary to trigger water condensation at the surface are 0.1 $M_{EO}$ and 0.06 $M_{EO}$ for Trappist-1e and Trappist-1f, respectively. These values are quite low and open the discussion on whether water has condensed in the past on these planets and if some liquid water would still be present on their surface.

Despite all the caveats already pointed out, we believe that our approach using a 1D coupled MO model is useful to better understand the repartition of volatiles between interiors and atmospheres, an important point to explain the observations and to discriminate between different types of exoplanets interior compositions, as exemplified in the recent publication of Luque and Palle (2022).

## 5. Conclusion

We present an update of our model for the thermal evolution of a MO in interaction with a degassing atmosphere of $H_2O$ and $CO_2$. A new equation for the mass balance of volatiles is implemented, correcting Salvador et al., 2017. The main conclusions are qualitatively unchanged. In particular, the time necessary to reach the ERCS remains essentially the same as in S2017. Moreover, this update increases the likelihood of early water ocean formation on

rocky planets. On early Venus, 0.13 Earth's ocean mass might be sufficient to form a water ocean, depending on its cloud cover and resulting albedo. Our results applied to exoplanets suggest that liquid water might be present on the surface of Trappist-1e and 1f, provided that those planets volatile primitive content were dominated by $H_2O$ and $CO_2$. Comparing our results with other recent models, we discuss the relative influence of the model hypotheses, such as mantle melting curves (which depend on mantle composition), the treatment of the atmosphere (e.g., gray or convective-radiative, 1D or 3D) and the treatment of the last stages of the MO solidification (e.g., episodic resurfacing, stagnant lid…). Further work should explore other MO composition, solubility laws, different solidification scenarios and a more complete atmosphere treatment including escape.

## Data Availability Statement

Most of the parameter values can be found in S2017 since this version is a correction of the paper, it uses the same values of parameters and rheology. The source code of the interior model can be found in Massol et al. (2023a) and the data set for the calculations in Massol et al. (2023b). The source code of the atmospheric model can be found in the open data section of Marcq et al. (2017).

**Acknowledgments**
The authors acknowledge support from the Institut National des Sciences de l'Univers (INSU), the Centre National de la Recherche Scientifique (CNRS) and Centre National d'Etudes Spatiales (CNES) through the Programme National de Planétologie. The authors also acknowledge the two anonymous reviewers for their very interesting comments and suggestions that improved the manuscript.

## References

Abe, Y. (1997). Thermal and chemical evolution of the terrestrial magma ocean. *Physics of the Earth and Planetary Interiors*, *100*(1–4), 27–39. https://doi.org/10.1016/s0031-9201(96)03229-3

Abe, Y., Abe-Ouchi, A., Sleep, N., & Zahnle, K. (2011). Habitable zone limits for dry planets. *Astrobiology*, *11*(5), 443–460. https://doi.org/10.1089/ast.2010.0545

Andrault, D., Bolfan-Casanova, N., Nigro, G. L., Bouhifd, M. A., Garbarino, G., & Mezouar, M. (2011). Solidus and liquidus profiles of chondritic mantle: Implication for melting of the Earth across its history. *Earth and Planetary Science Letters*, *304*(1–2), 251–259. https://doi.org/10.1016/j.epsl.2011.02.006

Avice, G., Parai, R., Jacobson, S., Labidi, J., Trainer, M., & Petkov, M. (2022). Noble gases and stable isotopes track the origin and early evolution of the Venus atmosphere. *Space Science Reviews*, *218*(8), 60. https://doi.org/10.1007/s11214-022-00929-9

Bahcall, J. N., Pinsonneault, M. H., & Basu, S. (2001). Solar models: Current epoch and time dependences, neutrinos, and helioseismological properties. *The Astrophysical Journal*, *555*(2), 990–1012. https://doi.org/10.1086/321493

Boukrouche, R., Lichtenberg, T., & Pierrehumbert, R. T. (2021). Beyond runaway: Initiation of the post-runaway greenhouse state on rocky exoplanets. *The Astrophysical Journal*, *919*(2), 130. https://doi.org/10.3847/1538-4357/ac1345

Bower, D. J., Hakim, K., Sossi, P. A., & Sanan, P. (2022). Retention of water in terrestrial magma oceans and carbon-rich early atmospheres. *The Planetary Science Journal*, *3*(4), 93. https://doi.org/10.3847/PSJ/ac5fb1

Bower, D. J., Kitzmann, D., Wolf, A. S., Sanan, P., Dorn, C., & Oza, V. A. (2019). Linking the evolution of terrestrial interiors and an early outgassed atmosphere to astrophysical observations. *Astronomy & Astrophysics*, *631*, A103. https://doi.org/10.1051/0004-6361/201935710

Cadieux, C., Doyon, R., Plotnykov, M., Hébrard, G., Jahandar, F., Artigau, É., et al. (2022). Toi-1452 b: SPIRou and TESS reveal a super-earth in a temperate orbit transiting an M4 dwarf. *The Astronomical Journal*, *164*(3), 96. https://doi.org/10.3847/1538-3881/ac7cea

Carter, J. A., Agol, E., Chaplin, W. J., Basu, S., Bedding, T. R., Buchhave, L. A., et al. (2012). Kepler-36: A pair of planets with neighboring orbits and dissimilar densities. *Science*, *337*(6094), 556–559. https://doi.org/10.1126/science.1223269

Chaverot, G., Turbet, M., Bolmont, E., & Leconte, J. (2022). How does the background atmosphere affect the onset of the runaway greenhouse? *Astronomy & Astrophysics*, *658*, A40. https://doi.org/10.1051/0004-6361/202142286

Del Genio, A. D., Kiang, N. Y., Way, M. J., Amundsen, D. S., Sohl, L. E., Fujii, Y., et al. (2019). Albedos, equilibrium temperatures, and surface temperatures of habitable planets. *The Astrophysical Journal*, *884*(1), 75. https://doi.org/10.3847/1538-4357/ab3be8

Donahue, T. M., Hoffman, J. H., Hodges, R. R., & Watson, A. J. (1982). Venus was wet: A measurement of the ratio of deuterium to hydrogen. *Science*, *216*(4546), 630–633. https://doi.org/10.1126/science.216.4546.630

Dorn, C., & Lichtenberg, T. (2021). Hidden water in magma ocean exoplanets. *The Astrophysical Journal Letters*, *922*(1), L4. https://doi.org/10.3847/2041-8213/ac33af

Elkins-Tanton, L. T. (2008). Linked magma ocean solidification and atmospheric growth for earth and mars. *Earth and Planetary Science Letters*, *271*(1), 181–191. https://doi.org/10.1016/j.epsl.2008.03.062

Forget, F., & Pierrehumbert, R. (1997). Warming early mars with carbon dioxide clouds that scatter infrared radiation. *Science*, *278*(5341), 1273–1276. https://doi.org/10.1126/science.278.5341.1273

Gaillard, F., Bernadou, F., Roskosz, M., Bouhifd, M., Marrocchi, Y., Iacono-Marziano, G., et al. (2022). Redox controls during magma ocean degassing. *Earth and Planetary Science Letters*, *577*, 117255. https://doi.org/10.1016/j.epsl.2021.117255

Gaillard, F., Bouhifd, M. A., Füri, E., Malavergne, V., Marrocchi, Y., Noack, L., et al. (2021). The diverse planetary ingassing/outgassing paths produced over billions of years of magmatic activity. *Space Science Reviews*, *217*(1), 22. https://doi.org/10.1007/s11214-021-00802-1

Gillmann, C., Way, M., Avice, G., Breuer, D., Golabek, G., Honing, D., et al. (2022). The long-term evolution of the atmosphere of Venus: Processes and feedback mechanisms interior-exterior exchanges. *Space Science Reviews*, *218*(7), 56. https://doi.org/10.1007/s11214-022-00924-0

Graham, R. J., Lichtenberg, T., Boukrouche, R., & Pierrehumbert, R. T. (2021). A multispecies pseudoadiabat for simulating condensable-rich exoplanet atmospheres. *The Planetary Science Journal*, *2*(5), 207. https://doi.org/10.3847/PSJ/ac214c

Grimm, S., Demory, B., Gillon, M., Dorn, C., Agol, E., Burdanov, A., et al. (2018). The nature of the TRAPPIST-1 exoplanets. *Astronomy & Astrophysics*, *613*, A68. https://doi.org/10.1051/0004-6361/201732233

Gronoff, G., Arras, P., Baraka, S., Bell, J. M., Cessateur, G., Cohen, O., et al. (2020). Atmospheric escape processes and planetary atmospheric evolution. *Journal of Geophysical Research: Space Physics*, *125*(8), e2019JA027639. https://doi.org/10.1029/2019JA027639

Gough, D. O. (1981). Solar interior structure and luminosity variations. *Solar Physics*, *74*(1), 21–34. https://doi.org/10.1007/bf00151270

Hamano, K., Abe, Y., & Genda, H. (2013). Emergence of two types of terrestrial planet on solidification of magma ocean. *Nature*, *497*(7451), 607–610. https://doi.org/10.1038/nature12163

Hamano, K., Kawahara, H., Abe, Y., Onishi, M., & Hashimoto, G. L. (2015). Lifetime and spectral evolution of a magma ocean with a steam atmosphere: Its detectability by future direct imaging. *The Astrophysical Journal*, *806*(2), 216. https://doi.org/10.1088/0004-637X/806/2/216
Hier-Majumder, S., & Hirschmann, M. (2017). The origin of volatiles in the earth's mantle. *Geochemistry, Geophysics, Geosystems*, *18*(8), 3078–3092. https://doi.org/10.1002/2017GC006937
Kasting, J. F. (1988). Runaway and moist greenhouse atmospheres and the evolution of Earth and Venus. *Icarus*, *74*(3), 472–494. https://doi.org/10.1016/0019-1035(88)90116-9
Koll, D. (2022). A scaling for atmospheric heat redistribution on tidally locked rocky planets. *The Astrophysical Journal*, *924*(2), 134. https://doi.org/10.3847/1538-4357/ac3b48
Kopparapu, R. K., Ramirez, R., Kasting, J. F., Eymet, V., Robinson, T. D., Mahadevan, S., et al. (2013). Habitable zones around main-sequence stars: New estimates. *The Astrophysical Journal*, *770*(1), 82. https://doi.org/10.1088/0004-637X/770/1/82
Krasnopolsky, V., Belyaev, D., Gordon, I., Li, G., & Rothman, L. (2013). Observations of D/H ratios in $H_2O$, HCl, and HF on Venus and new DCl and DF line strengths. *Icarus*, *224*(1), 57–65. https://doi.org/10.1016/j.icarus.2013.02.010
Krissansen-Totton, J., Fortney, J., & Nimmo, F. (2021). Was Venus ever habitable? Constraints from a coupled interior-atmosphere-redox evolution model. *Planetary Science Journal*, *2*(5), 216. https://doi.org/10.3847/PSJ/ac2580
Krissansen-Totton, J., Galloway, M., Wogan, N., Dhaliwal, J., & Fortney, J. (2021). Waterworlds probably do not experience magmatic outgassing. *The Astrophysical Journal*, *913*(2), 107. https://doi.org/10.3847/1538-4357/abf560
Labrosse, S., Hernlund, J. W., & Coltice, N. (2007). A crystallizing dense magma ocean at the base of the Earth's mantle. *Nature*, *450*(7171), 866–869. https://doi.org/10.1038/nature06355
Lebrun, T., Massol, E., Chassefiere, H., Davaille, A., Marcq, E., Sarda, P., et al. (2013). Thermal evolution of an early magma ocean in interaction with the atmosphere. *Journal of Geophysical Research: Planets*, *118*(6), 1155–1176. https://doi.org/10.1002/jgre.20068
Leconte, J., Forget, F., Charnay, B., Wordsworth, R., Selsis, F., Millour, E., & Spiga, A. (2013). 3D climate modeling of close-in land planets: Circulation patterns, climate moist bistability, and habitability. *Astronomy & Astrophysics*, *554*, A69. https://doi.org/10.1051/0004-6361/201321042
Lichtenberg, T. (2021). Redox hysteresis of super-earth exoplanets from magma ocean circulation. *The Astrophysical Journal Letters*, *914*(1), L4. https://doi.org/10.3847/2041-8213/ac0146
Lichtenberg, T., Bower, D., Hammond, M., Boukrouche, R., Sanan, P., Tsai, S., & Pierrehumbert, R. (2021). Vertically resolved magma ocean-protoatmosphere evolution: $H_2$, $H_2O$, $CO_2$, $CH_4$, CO, $O_2$, and $N_2$ as primary absorbers. *Journal of Geophysical Research: Planets*, *126*(2), e2020JE006711. https://doi.org/10.1029/2020JE006711
Luque, R., & Palle, E. (2022). Density, not radius, separates rocky and water-rich small planets orbiting M dwarf stars. *Science*, *377*(6611), 1211–1214. https://doi.org/10.1126/science.abl7164
Marcq, E., Salvador, A., Massol, H., & Davaille, A. (2017). Thermal radiation of magma ocean planets using a 1D radiative-convective model of $H_2O$-$CO_2$ atmospheres. *Journal of Geophysical Research: Planets*, *122*(7), 1539–1553. https://doi.org/10.1002/2016JE005224
Massol, H., Davaille, A., & Sarda, P. (2023a). 1D model for thermal evolution of a magma ocean containing $H_2O$ and $CO_2$. https://doi.org/10.5281/zenodo.8087205
Massol, H., Davaille, A., & Sarda, P. (2023b). Dataset associated with Massol et al., 2023. https://doi.org/10.5281/zenodo.8086570
Meier, T. G., Bower, D. J., Lichtenberg, T., Tackley, P. J., & Demory, B.-O. (2021). Hemispheric tectonics on super-earth LHS 3844b. *The Astrophysical Journal Letters*, *908*(2), L48. https://doi.org/10.3847/2041-8213/abe400
Miyazaki, Y., & Korenaga, J. (2022). Inefficient water degassing inhibits ocean formation on rocky planets: An insight from self-consistent mantle degassing models. *Astrobiology*, *22*(6), 713–734. https://doi.org/10.1089/ast.2021.0126
Monteux, J., Andrault, D., Guitreau, M., Samuel, H., & Demouchy, S. (2020). A mushy earth's mantle for more than 500 Myr after the magma ocean solidification. *Geophysical Journal International*, *221*(2), 1165–1181. https://doi.org/10.1093/gji/ggaa064
Nikolaou, A., Katyal, N., Tosi, N., Godolt, M., Grenfell, J. L., & Rauer, H. (2019). What factors affect the duration and outgassing of the terrestrial magma ocean? *The Astrophysical Journal*, *875*(1), 11. https://doi.org/10.3847/1538-4357/ab08ed
Owen, J. E., Shaikhislamov, I. F., Lammer, H., Fossati, L., & Khodachenko, M. L. (2020). Hydrogen dominated atmospheres on terrestrial mass planets: Evidence, origin and evolution. *Space Science Reviews*, *216*(8), 129. https://doi.org/10.1007/s11214-020-00756-w
Patocka, V., Calzavarini, E., & Tosi, N. (2020). Settling of inertial particles in turbulent Rayleigh-Benard convection. *Physical Review Fluids*, *5*(11), 114304. https://doi.org/10.1103/PhysRevFluids.5.114304
Patocka, V., Tosi, N., & Calzavarini, E. (2022). Residence time of inertial particles in 3D thermal convection: Implications for magma reservoirs. *Earth and Planetary Science Letters*, *591*, 117622. https://doi.org/10.1016/j.epsl.2022.117622
Pierrehumbert, R. T. (2010). *Principles of planetary climate*. Cambridge University Press. https://doi.org/10.1017/CBO9780511780783
Pierrehumbert, R. T. (2023). The runaway greenhouse on sub-Neptune waterworlds. *The Astrophysical Journal*, *944*(1), 20. https://doi.org/10.3847/1538-4357/acafdf
Ryan, D. J., & Robinson, T. D. (2022). Detecting oceans on exoplanets with phase-dependent spectral principal component analysis. *The Planetary Science Journal*, *3*(2), 33. https://doi.org/10.3847/PSJ/ac4af3
Salvador, A., Massol, H., Davaille, A., Marcq, E., Sarda, P., & Chassefiere, E. (2017). The relative influence of $H_2O$ and $CO_2$ on the primitive surface conditions and evolution of rocky planets. *Journal of Geophysical Research: Planets*, *122*(7), 1458–1486. https://doi.org/10.1002/2017JE005286
Salvador, A., & Samuel, H. (2023). Convective outgassing efficiency in planetary magma oceans: Insights from fluid. *Icarus*, *390*, 115265. https://doi.org/10.1016/j.icarus.2022.115265
Schaefer, L., Wordsworth, R. D., Berta-Thompson, Z., & Sasselov, D. (2016). Predictions of the atmospheric composition of GJ 1132b. *The Astrophysical Journal*, *829*(2), 63. https://doi.org/10.3847/0004-637X/829/2/63
Spiegel, E. A. (1963). A generalization of the mixing-length theory of turbulent convection. *The Astrophysical Journal*, *138*, 216. https://doi.org/10.1086/147628
Turbet, M., Bolmont, E., Chaverot, G., Ehrenreich, D., Leconte, J., & Marcq, E. (2021). Day–night cloud asymmetry prevents early oceans on Venus but not on earth. *Nature*, *598*(7880), 276–280. https://doi.org/10.1038/s41586-021-03873-w
Way, M., & Del Genio, A. (2020). Venusian habitable climate scenarios: Modeling Venus through time and applications to slowly rotating Venus-like exoplanets. *Journal of Geophysical Research: Planets*, *125*(5), e2019JE006276. https://doi.org/10.1029/2019JE006276
Way, M., Del Genio, A. D., Kiang, N. Y., Sohl, L. E., Grinspoon, D. H., Aleinov, I., et al. (2016). Was Venus the first habitable world of our solar system? *Geophysical Research Letters*, *43*(16), 8376–8383. https://doi.org/10.1002/2016GL069790
Windsor, J., Robinson, T., Kopparapu, R., Young, A., Trilling, D., & LLama, J. (2023). A radiative-convective model for terrestrial planets with self-consistent patchy clouds. *Planetary Science Journal*, *4*(5), 94. https://doi.org/10.3847/PSJ/acbf2d
Wordsworth, R., & Kreidberg, L. (2022). Atmospheres of rocky exoplanets. *Annual Review of Astronomy and Astrophysics*, *60*(1), 159–201. https://doi.org/10.1146/annurev-astro-052920-125632

Yang, J., Boué, G., Fabrycky, D. C., & Abbot, D. S. (2014). Strong dependence of the inner edge of the habitable zone on planetary rotation rate. *The Astrophysical Journal Letters*, *787*(1), L2. https://doi.org/10.1088/2041-8205/787/1/L2

Yang, J., Leconte, J., Wolf, E., Merlis, T., Koll, D., Forget, F., & Abbot, D. (2019). Simulations of water vapor and clouds on rapidly rotating and tidally locked planets: A 3D model intercomparison. *The Astrophysical Journal*, *875*(1), 46. https://doi.org/10.3847/1538-4357/ab09f1